PERSPECTIVE

Check for updates

Emerging techniques and scenarios of scanning electrochemical microscopy for the characterization of electrocatalytic reactions

Jinming Xu, Ran Chen, [ID] * Juanxian Song, Songqin Liu, [ID] Yanfei Shen [ID] and Yuanjian Zhang [ID]

To fulfill the evergrowing energy consumption demands and the pursuit of sustainable and renewable energy, electrocatalytic reactions such as the water electrocatalysis reaction, the O_2 reduction reaction, the N_2 reduction reaction (NRR), the CO_2 reduction reaction (CO_2RR), *etc.*, have drawn a lot of attention. Scanning electrochemical microscopy (SECM) is a powerful technique for *in situ* surface characterization, providing critical information about the local reactivity of electrocatalysts and unveiling key information about the reaction mechanisms, which are essential for the rational design of novel electrocatalysts. There has been a growing trend of SECM-based studies in electrocatalytic reactions, with a major focus on water splitting and O_2 reduction reactions, and relying mostly on conventional SECM techniques. Recently, novel operation modes of SECM have emerged, adding new features to the functionality of SECM and successfully expanding the scope of SECM to other electrocatalytic reactions, *i.e.*, the NRR, the NO_3^- reduction reaction (NO_3RR), the CO_2RR and so on, as well as more complicated electrolysis systems, *i.e.* gas diffusion electrodes. In this perspective, we summarized recent progress in the development of novel SECM techniques and recent SECM-based research studies on the NRR, NO_3RR, CO_2RR, and so on, where quantitative information on the reaction mechanism and catalyst reactivity was uncovered through SECM. The development of novel SECM techniques and the application of these techniques can provide new insights into the reaction mechanisms of diverse electrocatalytic reactions as well as the *in situ* characterization of electrocatalysts, facilitating the pursuit of sustainable and renewable energy.
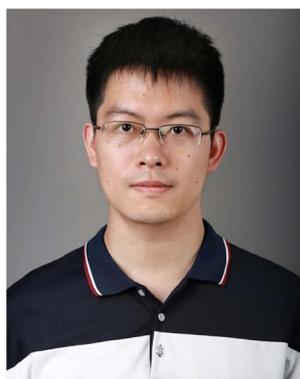
Jiangsu Province Key Laboratory of Critical Care Medicine, Jiangsu Engineering Laboratory of Smart Carbon-Rich Materials and Device, Jiangsu Province Hi-Tech Key Laboratory for Bio-Medical Research, School of Chemistry and Chemical Engineering, Southeast University, Nanjing, 211189, China. E-mail: rchen@seu.edu.cn

Jinming Xu received his BS in chemistry from Yangzhou University in 2023 and is currently a master's student under the supervision of Prof. Ran Chen and Prof. Yuanjian Zhang. He is currently focusing on reactive oxygen species detection using nanopipet-supported interfaces between two immiscible electrolytes (nano-ITIES) and scanning electrochemical microscopy, and his research interests include ultra-microeletrodes, the oxygen reduction reaction and molecular sensing.

Jinming Xu

Ran Chen received his BS from Nanjing University in 2010, and completed his PhD in Chemistry at the University of Pittsburgh in 2017 under the supervision of Prof. S. Amemiya. After graduation, he worked as a post-doctoral research associate in Prof. M. Shen's group at the University of Illinois at Urbana-Champaign from 2017 to 2020. He is currently an associate professor at the School of Chemistry and Chemical Engineering in Southeast University, China. His research interest focused on the electrochemical characterization of reaction mechanisms using ultramicroelectrodes.

Ran Chen

Introduction

The pollution issues and greenhouse effects caused by fossil fuels as well as the ever-growing demand for energy have become a worldwide concern.[1–4] Thus, the pursuit of sustainable and renewable energy, and the utilization of this energy, has drawn lots of attention.[5–10] Electrocatalytic reactions driven by electricity generated through wind power, tidal power, solar power, *etc.*, play crucial roles in the field of sustainable and renewable energy generation and utilization.[11–14] For example, the water electrolysis reaction, one of the most-studied electrocatalytic reactions, is vital for hydrogen power generation.[15–17] The carbon dioxide reduction reaction (CO_2RR) can convert CO_2 in the atmosphere into organic products.[18–20] The nitrate reduction reaction (NO_3RR) helps to convert the nitrogen pollutant in industrial and agriculture wastewater into value-added ammonia products.[21–23] As a result, several core electrocatalytic reactions have triggered a great deal of research.[24–28]

Comprehensive knowledge of various complicated processes at the catalyst interface during an electrocatalytic reaction, including the adsorption and desorption process, the electron transfer process, solvation and desolvation behaviors, electrostatic interactions, *etc.*, is crucial for the engineering and optimization of electrocatalytic systems as well as for the rational design of novel electrocatalysts. The structural and chemical characteristics of electrocatalysts can be examined using various characterization methods, including scanning electron microscopy-energy dispersive X-ray spectrometry (SEMEDS), X-ray photoelectron spectroscopy (XPS), UV-vis fluorescence microscopy, Raman spectroscopy and so on.[29] On the other hand, conventional electrochemical techniques such as cyclic voltammetry (CV) and electrochemical impedance spectroscopy (EIS) are widely used in the study of electrocatalytic reactions, capturing the average electrochemical properties of the catalysts.[30,31] However, since electrocatalysts are often spatially heterogeneous due to surface features at the microscopic level, *i.e.*, surface defects, various crystalline facets and phases, non-uniform catalyst distribution, *etc.*,[32–35] an electrochemical technique with high spatial resolution is critical for characterizing the local reactivity at different microscopic regions and unraveling the complicated reaction processes during electrolysis.

Scanning electrochemical microscopy (SECM) is a powerful and versatile technique for *in situ* surface characterization with high spatial and temporal resolution.[36–39] Using nanoelectrodes as the probe, a lateral spatial resolution ~10 nm and a horizontal tip–substrate distance of a few nanometers on flat substrates have been achieved, enabling the detection of short-lived intermediates and the analysis of ultrafast reaction kinetics near the substrate.[40–43] Due to its high spatial resolution, *in situ* operation modes, and versatile functionality, SECM has also been widely used in various fields, such as studying complicated reaction mechanisms, characterizing the local morphology and reactivity at the electrode surface, probing cellular activity, *etc.*[36,44–48] There is a growing trend of SECM-based studies in electrocatalytic reactions, where critical information on the local reactivity at different microscopic regions on an electrocatalytic material was revealed using SECM.[43,49,50] The majority of these studies focused on water splitting and O_2 reduction reactions,[51–60] and traditional SECM operation techniques, namely, the feedback mode and the generation/collection mode, were used to quantify the localized reactivity.[61–63] Additionally, since a flat electrode surface was required for positioning the probe close and carrying out accurate SECM measurements, these SECM-based studies were often limited to two-dimensional planar materials.[64,65]

Recently, novel operation modes of SECM have emerged, adding new features to the functionality of SECM.[66–72] For example, the surface interrogation mode enabled the quantification of active sites on catalytic surfaces,[66,67] and sequential voltammetric SECM (SV-SECM) permits the simultaneous identification of numerous species under complicated working conditions and provided the capability for mapping facet-dependent products selectively,[68] while shear-force-based and capacitance-based approach curves allowed for the positioning of probes near non-flat surfaces.[69–72] These new techniques helped to expand the scope of SECM to other electrocatalytic reactions, *i.e.*, the N_2 reduction reaction (NRR), NO_3RR, CO_2RR, and so on, as well as more complicated electrolysis systems, such as the gas diffusion electrode (GDE). Thus, in this perspective, the recent development of novel SECM techniques was first summarized, followed by the recent SECM-based research on the NRR, NO_3RR, CO_2RR, and so on, where quantitative information on the reaction mechanism and catalyst reactivity was uncovered through SECM.

Yuanjian Zhang received his BS from Nanjing University in 2002 and completed his PhD at the Changchun Institute of Applied Chemistry, Chinese Academy of Sciences in 2007. Subsequently, he joined the Max-Planck Institute of Colloids and Interfaces (Germany) as a postdoctoral researcher. From 2009–2012, he worked at the National Institute for Materials Science (Japan) as an ICYS researcher. He joined the faculty at Southeast University (China) in 2012 as a Professor of Chemistry. He is interested in carbosensing (carbon matter-derived optoelectronic sensors), and has expertise in electroanalytical chemistry, electrochemiluminescence, electrocatalysis, photocatalysis and photoelectrochemistry.

Yuanjian Zhang

Recent progress in novel SECM operative modes

Surface interrogation mode

Although first introduced in 2008,[73,74] the surface interrogation (SI) mode of SECM has regained a lot of interest in the field of

electrocatalysis recently,[59,66,75,76] as it allowed for the study of active site densities and reaction kinetics where adsorbents are involved.

The working principle of the SI mode is shown in Fig. 1a–d. An UME serves as the probe to 'interrogate' the substrate surface coated with electrocatalysts by electrochemical titration. A redox mediator O is dispersed in solution, which can be reduced to R through a simple electron transfer reaction O + e → R at the biased UME surface, and when the substrate is under open circuit potential (OCP), R cannot convert back to O on the substrate. However, with the species A adsorbed at the active sites on the electrocatalyst surface, R can react with A to regenerate O, leading to a feedback current on UME, until all of the A species have reacted with R (Fig. 1b).[77] This way, the amount of A on the electrocatalyst surface can be electrochemically titrated by monitoring the feedback current on the UME, leading to a quantification of the active site density on the electrocatalyst surface. Additionally, if there are other competing processes on the active sites, such as the adsorption of another species B (Fig. 1c), the surface concentration of A will change with time. By varying the delay time before the titration, the time-dependent surface concentration of A can be quantified, leading to kinetic information of the adsorption rate of B (Fig. 1d). Note that a substrate comparable in size to the UME is usually required for accurate measurement of adsorbates to minimize the possible interference from lateral charge transfer effects.

Novel principles for carrying out approach curves

Prior to SECM measurements, the SECM probe (also known as the tip) was positioned near the substrate surface through the approach curve. Conventionally, the approach curve relies on the feedback effect where the diffusion towards the tip is interfered with by the substrate as the tip–substrate distance gets shorter, *i.e.* around the same magnitude as the size of the tip. The conventional approach curves prefer substrates with superior flatness, and are conducted in the aqueous phase, limiting the application of SECM when a rough substrate coated with catalysts or a solid/gas interface is under investigation. Recently, new principles for carrying out the approach curves have been proposed that address the above issues,[69–72] namely shear-force-based and capacitance-based approach curves.

Shear force, a type of short-range hydrodynamic force that exists only a few hundred nanometers away from solid surfaces,[78] lays the foundation for shear-force-based approach curves. During the shear-force-based approach curves, a resonantly oscillating tip is moving towards the substrate by a piezo with the oscillating magnitude monitored. When far from the substrate, the oscillating magnitude on the tip barely changes, yet once the tip–substrate distance is within the range of the shear force, the oscillation characteristics of the tip are modulated by the force, indicating a successful approach to the substrate (Fig. 1e). Since the shear-force is present regardless of the surface flatness, the shear-force based approach curve could work on electrodes with non-ideal flatness.

Another alternative method to carry out the approach curve relies on capacitance measurements in air.[70–72] By applying an AC voltage (typically 10 kHz, 1.4 V_{RMS}) on the substrate, a capacitive current can be generated on the tip. Considering the UME near a substrate as a system with a point charge positioned in front of a parallel-plate, the tip–substrate distance-dependent capacitance can be described by using eqn (1):

$$C_{tot}(Z) = -A_1 \times \ln(d_0 - Z) + B + \left(\frac{A_2}{L_{par} + d_0 - Z} \right) \quad (1)$$

where d_0 is the absolute surface position, Z is the position of the tip varied during the approach, $C_{tot}(Z)$ is the capacitance on the tip at position Z, A_1, A_2, and B are constant parameters related to experimental conditions and the electrochemical system and
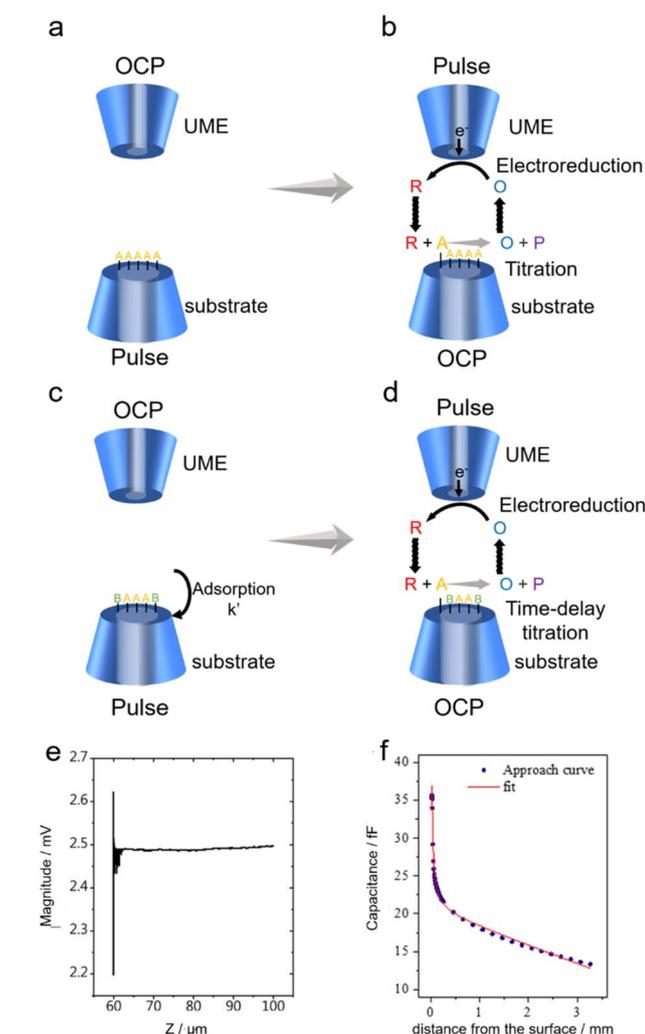

Fig. 1 (a–d) Schematic diagrams of SECM operation in SI mode. P represents the byproduct of the reaction between R and A. B is a substance that competes with A for adsorption on the substrate. (e) Shear forced based approach curve. Reproduced with permission from ref. 69, Royal Society of Chemistry, 2021. (f) Capacitive approach curve obtained (blue circles) with its fit to the theoretical result (red line). Reproduced with permission from ref. 71, American Chemical Society, 2019.

L_{par} is the length of the parallel-plate. A typical capacitance-based approach curve is shown in Fig. 1f, where the capacitive current generated on the tip is recorded as the tip approaches the substrate using a stepper motor. As the tip gets close to the substrate, the capacitance quickly increases, and through fitting the experimental approach curve with eqn (1), an accurate tip–substrate distance can be extracted. Note that the capacitance measurement is conducted in air, and thus this mode allows for the positioning of a UME towards a solid/gas interface.

Novel SECM technique-based study of electrocatalytic reactions

SI-SECM-based NRR study

Over the past century, the Haber–Bosch process, which contributes annually to over 90% of the world's ammonia production, has powered the chemical synthesis of ammonia and fed billions of people. Due to its heavy reliance on fossil fuels, this process actually consumes around 2% of the total anthropogenic energy and emits 400 million tons of CO_2 annually.[79–81] The synthesis of ammonia by electrocatalysis offers the potential to operate on renewable electricity under ambient conditions with no carbon footprint, and has garnered lots of attention recently.[82–85] NH_3 synthesis through the electrochemical NRR is becoming a viable substitute for the traditional Haber–Bosch fertilizer industry.[86–88] Vast amounts of efforts have been devoted to the development of stable and effective catalysts for the NRR, particularly earth-abundant non-precious transition metal (TM)-based materials such as metallic oxides, sulphides, nitrides, and carbides.[89–91] However, under acidic conditions, the abundance of protons in the solution causes an increased competition with the hydrogen evolution reaction (HER), posing a problem of reaction selectivity.

A novel type of TiO_2 nanoreactor with surface strain was proposed by Li and colleagues, which allowed for the synthesis of ammonia with high selectivity.[92] TiO_2 nanotube arrays (TiO_2 NTs) were first created by anodizing Ti plates twice, followed by annealing to form anatase TiO_2. The electrochemical intercalation of Li ions and the follow-up delithiation created lattice strain (s-TiO_2 NTs). The structural and chemical environments of TiO_2 nanoreactors were examined using X-ray diffraction (XRD) and high-resolution transmission electron microscopy (TEM) to confirm the presence of lattice strain (Fig. 2a–d). Then the authors studied the NRR activity of the TiO_2 NTs by applying −0.5 V on the TiO_2 nanoreactors for 2 hours, and monitored the NH_3 production through UV/vis absorption using the indophenol blue indicator. As shown in Fig. 2e, compared to TiO_2 NTs, the tailored s-TiO_2 NTs delivered improved performance for the conversion of nitrogen to ammonia. It was discovered that s-TiO_2 exhibited 26% higher faradaic efficiency compared to TiO_2 NTs. To better understand this strain-induced increase in NRR efficiency, the active site densities on TiO_2 and s-TiO_2 were quantified using the SI-SECM approach (Fig. 2f). Two identical 50 μm-diameter glass-sealed platinum UMEs served as the tip and substrate electrodes. Using a tip-generated titrant (ferrocenium, Fc^+), the amount of the active species, Ti^{3+} on the
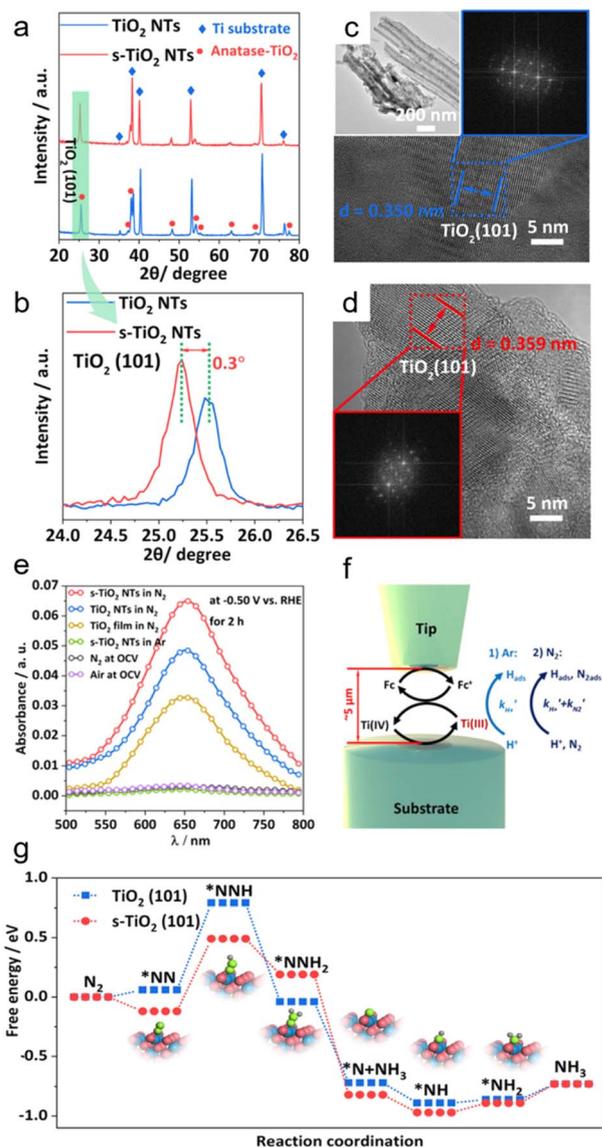

Fig. 2 (a and b) XRD patterns of TiO_2 NTs and s-TiO_2 NTs. (c and d) TEM images and the corresponding fast Fourier transform (FFT) patterns (the inset) of TiO_2 NTs (c) and s-TiO_2 NTs (d). (e) UV/vis absorption spectra of the electrolyte with an indophenol indicator after 2 h of electrolysis at −0.5 V. (f) Illustration of SI-SECM for determining the reaction rate constants of H^+ and N_2 adsorption on the Ti^{3+} site in TiO_2 NTs and s-TiO_2 NTs. (g) DFT-calculated pathways of the NRR through the distal mechanisms on pristine and strained TiO_2 (101). Reproduced with permission from ref. 92, John Wiley and Sons, 2020.

surface of the catalyst was analyzed. More precisely, the substrate was first biased at a reduction potential $E_{substrate}$ for 20 s to convert all the Ti^{4+} at the active sites to Ti^{3+}. Then the substrate was biased at OCP, the tip was biased to oxidize Fc to Fc^+, and the chronoamperometric curve on the tip was recorded. At the substrate, Ti^{3+} on the catalyst surface would reduce Fc^+ to Fc, which was then oxidized on the tip, causing feedback current signals on the tip until all of the Ti^{3+} was used up. Thus, by integrating the charges in the chronoamperometric curve, the precise amount of Ti^{3+} generated at $E_{substrate}$ was

determined. Similarly, the reaction rate constants for the H^+ (k'_{H^+}) and N_2 (k'_{N_2}) binding on TiO_2 NTs and s-TiO_2 NTs were determined, by adding a delay time t_d before the titration, and tracking the remaining Ti^{3+} after Ti^{3+} had reacted with N_2 and H^+ for a duration of t_d. The outcome indicated that both k'_{N_2} and k'_{H^+} exhibited characteristics of a pseudo-first-order process. Specifically, k'_{N_2} for s-TiO_2 NTs (0.62 s^{-1}) was almost twice that on TiO_2 NTs (0.32 s^{-1}), suggesting that N_2 adsorption on s-TiO_2 NTs was more advantageous than on TiO_2 NTs. Additionally, the k'_{H^+} adsorption on s-TiO_2 was weaker compared with k'_{N_2}, explaining the good selectivity towards NH_3 production observed on s-TiO_2. The difference in the k'_{N_2} and k'_{H^+} observed on TiO_2 and s-TiO_2 was also supported by density functional theory (DFT) calculations (Fig. 2g).

Besides the SI-SECM technique, conventional SECM modes like SG/TC and SECM imaging have also been utilized in NRR study. Park *et al.* evaluated NRR electrocatalysis on a Fe–CuS/C electrode by *in situ* detection of NH_3 using SECM for the first time.[93] Conventionally, the activity of the NRR catalyst was estimated by the *ex situ* detection of NH_3 using spectrophotometric methods including Nessler reagent, indophenol, salicylic acid reactions, *etc.* Additionally, liquid chromatography, ion chromatography, and a rotating ring-disc electrode (RRDE) were also commonly used for *ex situ* NH_3 detection.[94] To enable the *in situ* detection of NH_3, the authors fabricated a polycrystalline Pt UME through thermochemical deposition of Pt on an unmodified Pt UME ($d = 25$ μm), and carried out CV measurements of the ammonia oxidation reaction (AOR) in solutions with different NH_3 concentrations (Fig. 3a). It was found that the modified Pt UME showed an enhanced tip current towards the AOR, which was due to the easier AOR kinetics and increased surface area caused by the deposited Pt nanoparticles, and a calibration curve of peak current at 0.71 V_{RHE} *versus* NH_3 concentration was established (Fig. 3b). The calibration curve was compared with the *ex situ* colorimetrical measurements using the indephenol method, and consistent results were obtained. Furthermore, the authors showed that the stability of NRR catalysts can be evaluated through real-time NH_3 detection using SECM, as presented in Fig. 3c. By locating the modified Pt UME close to the Fe–CuS/C electrode, the authors detected the NH_3 generated at the electrode *in situ* and found that during repetitive CV scans, the amount of NH_3 produced decreased, indicating a degrading process of the Fe–CuS/C electrode (Fig. 3d).

Nagaiah *et al.* prepared a Cu–Ni$_4$B$_3$ catalyst and investigated the competition between the NRR and HER using SECM.[95] The Cu–Ni$_4$B catalyst with a grape bunch-like morphology was synthesized by a one-step sonochemical reduction method, with Cu added to the surface of nickel boride in an effort to change the electronic structure and increase the activity of the electrocatalytic NRR. Electrocatalytic NRR activity measurement with a catalyst-coated glass carbon plate by chronoamperometry demonstrated that Cu–Ni$_4$B$_3$ (1 : 2) exhibited superior NRR activity in 0.1 M H_2SO_4 electrolyte compared to catalysts of other proportions. Nevertheless, the catalyst faced fierce competition from the HER in acidic environments, making it challenging to determine the absolute NRR activity using traditional *ex situ*
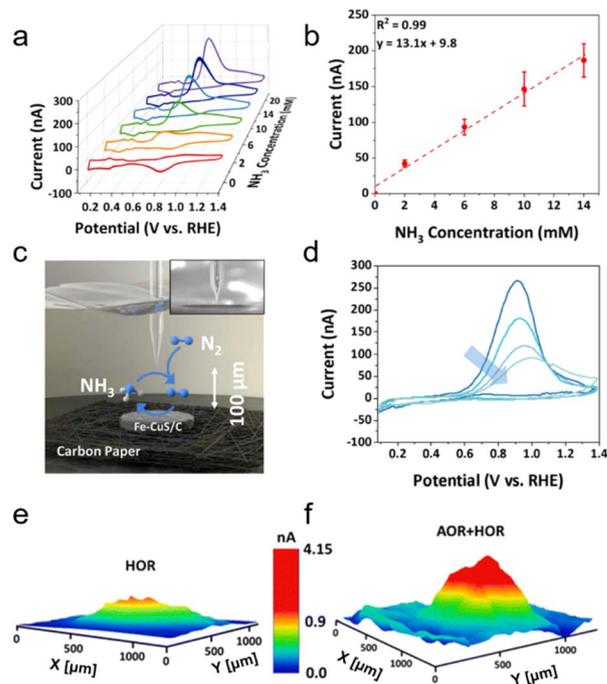

Fig. 3 (a) CVs of NH_3 oxidation at the modified Pt UME in 1 M KOH solution containing 0 to 20 mM NH_3. Scan rate: 20 mV s^{-1}. (b) The relationship between NH_3 concentration and the peak current of the AOR in 1 M KOH solution. (c) A schematic diagram of the study of the NRR on the Fe–CuS/C-loaded carbon paper with a Pt UME in the SECM SG-TC mode. The inset shows an actual image of the experimental setup. (d) Repetitive CVs of the AOR were collected at the Pt UME when the UME was positioned close to the Fe–CuS/C-loaded carbon paper. The carbon paper was biased at −0.2 V *vs.* RHE. Scan rate: 20 mV s^{-1}. Reproduced with permission from ref. 93, Elsevier, 2023. (e and f) Three-dimensional SECM image showing the local catalytic activity of Cu–Ni$_4$B$_3$ (1 : 2). The tip was biased at a potential of 1.1 V in (e) under an Ar atmosphere to quantify the HOR on the tip, and in (f) under a N_2 atmosphere to detect the products of both the HER and NRR. Reproduced with permission from ref. 95, Royal Society of Chemistry, 2023.

methods like gas chromatography and the RRDE. In order to quantify the NRR activity of the Cu–Ni$_4$B$_3$ (1 : 2) catalyst and investigate the competition from the HER, the *in situ* SG/TC mode of SECM was applied (Fig. 3e and f). The experiments were carried out in 0.1 M H_2SO_4 saturated under a N_2 and Ar atmosphere, respectively, with 1.1 V *vs.* RHE applied on the tip and −0.3 V applied on the substrate. At this tip potential, both the HOR and AOR could occur on the tip surface. Under an Ar atmosphere, the concentration of N_2 in the solution was negligible, so that the current signal corresponded to the HER on Cu–Ni$_4$B$_3$ (1 : 2) (Fig. 3e). However, when under a N_2 atmosphere, larger tip currents were observed, which was due to the AOR current as a result of the NRR on Cu–Ni$_4$B$_3$ (1 : 2) (Fig. 3f), leading to solid proof of the competition between the HER and NRR.

SI-SECM-based study of the NO$_3$RR

Apart from the NRR, the electroreduction of nitrate to ammonia (NO$_3$RR) has been proposed as an alternative method to

synthesize NH_3, considering the abundant nitrate (NO_3^-) in waste water.[96,97] Compared to the Haber-Bosch process, the NO_3RR is more effective and more efficient, opening the door to waste recycling and sustainable nutrient recovery. Because of this, this approach has garnered a lot of interest, and numerous SECM-based studies have been conducted on the reaction mechanisms and selectivity of the NO_3RR,[98–103] which also suffers from the competition from the HER in a similar manner to the NRR.

Yu's group constructed a new type of Cu single-atom-modified gel (Cu-SAG) for the NO_3RR and the nitrite-to-ammonia reduction reaction (NO_2RR) with reduced competition from the HER.[98] The Cu-SAGs were synthesized through pyrolysis of the hydrogel-based precursors, namely, supramolecularly cross-linked polypyrrole (PPy)–copper(II) phthalocyanine tetrasulfonate (CuPcTs). Afterwards, Brunauer–Emmett–Teller (BET) surface area analysis and scanning electron microscopy (SEM) were used to confirm the porous structure of the gel. Atomic resolution scanning transmission electron microscopy (STEM) was used to further identify the metallic substances. Afterwards, the electrochemical properties of Cu-SAGs were characterized by linear sweep voltammetry (LSV). The onset potential for the HER on Cu-SAGs was found to be around -0.7 V $vs.$ RHE, while the onset potential for NO_3^- reduction to NO_2^- and NO_2^- reduction to NH_4^+ was found to be around -0.5 V and -0.8 V, respectively. An enhanced Faraday efficiency for NH_3 ($\sim$78%) over H_2 ($\sim$20%) was observed, with a yield rate of $\sim$440 µg cm^{-1} h^{-1} for ammonia production. At more negative potentials (-0.9 V), the reduction of NO_2^- to NH_4^+ had a faradaic efficiency close to 100%. Additionally, a noteworthy enhancement in the yield rate of NO_2^- converting to NH_4^+ was also observed, reaching a maximum of 10.5 µg mL^{-1} at -0.9 V. This value was about three times greater than that of the NO_3RR under the same circumstances. These findings indicated a different path for the NO_2RR with minimal influence from the HER, considerably enhancing the faradaic efficiency and yield rate. To gain insight into the mechanism of the NO_3RR and NO_2RR, the authors investigated the adsorption rate constants of NO_3^-, NO_2^- and H_2O on Cu sites using the SI-SECM technique, and discovered a much higher rate constant for NO_2^- adsorption (1.98 s^{-1}) than that for NO_3^- (0.83 s^{-1}) and H_2O (0.06 s^{-1}). This result explained the enhanced activity of NO_3^- reducing to NO_2^- compared with the HER, and it was also consistent with the molecular dynamics (MD) and DFT simulations. Based on this, a pulse electrolysis method was designed, where a higher potential of -0.5 V was first applied for 1.0 s to accumulate NO_2^- near the catalyst surface to overwhelm the H_2O adsorption, and then a potential of -0.8 V was applied to reduce NO_2^- to NH_4^+. Through this pulse electrolysis method, the competition from the HER was heavily suppressed.

Yu and associates created a Cu single-atom alloy oxide nanowire (Ni_1Cu SAAO NW) catalyst modified with Ni-sites for converting nitrate to ammonia with high efficiency.[99] $Cu(OH)_2$ nanowires were first grown on copper mesh and then treated with a Ni ion exchange process to form Ni_1–$Cu(OH)_2$ NWs. The Ni_1–$Cu(OH)_2$ NWs were then annealed and electrochemically reduced to form Ni_1Cu SAAO (Fig. 4a), which was inspected by
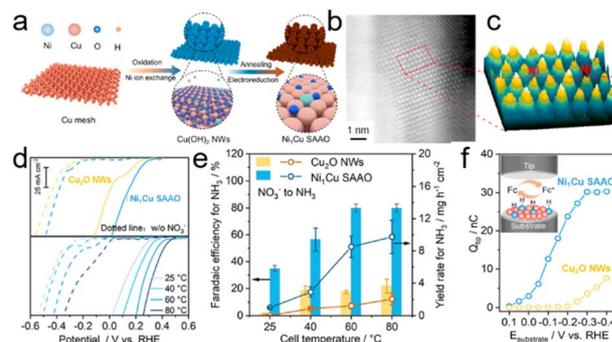

Fig. 4 (a) Schematic representation of the Ni_1Cu SAAO catalyst preparation process. (b) Atomic-resolution HAADF-STEM image of Ni_1Cu SAAO. (c) Local 3D topographic atom images for the region in (b). (d) LSVs of Ni_1Cu SAAO and Cu_2O NWs with and without adding NO_3^- in the electrolytes (top panel) as well as the LSVs at different cell temperatures (bottom panel). (e) Faradaic efficiency and yield rate of Ni_1Cu SAAO and Cu_2O NWs for the reduction of nitrate to ammonia at different cell temperatures at a potential of 0.1 V $vs.$ RHE. (f) Plots of tip-titration charges against substrate potential using SI-SECM for quantifying the concentration of surface-active hydrogen species on Cu_2O NWs and Ni_1Cu SAAO in 0.01 M KOH and 1.0 mM Fc. Reproduced with permission from ref. 99, American Chemical Society, 2024.

aberration-corrected high-angle annular dark-field scanning TEM (AC-HAADF-STEM) to acquire a more in-depth understanding of the Ni status in Ni_1Cu SAAO (Fig. 4b). A 3D topographic atom imaging analysis of the pixel intensity, as presented in Fig. 4c, made it evident that Ni atoms were located between Cu atoms and exhibited a single-atom distribution on the substrate. Significantly, LSV measurements showed that compared to Cu_2O NWs, the onset potential for the NO_3RR on Ni_1Cu SAAO was substantially less negative, suggesting that the NO_3RR was more advantageous on the Ni_1Cu SAAO catalyst (Fig. 4d). Furthermore, a clear peak of NO_2^- reduction was observed at 0.1 V $vs.$ RHE in Cu_2O NWs, yet this behavior was not observed on Ni_1Cu SAAO. This suggested that the Ni single atoms enabled the relay electrocatalysis of the NO_2^- intermediate product through the Ni site-generated active hydrogen species (*H). Additionally, as the cell temperature increased, the reaction rates of both the NO_3RR and HER on Ni_1Cu SAAO were enhanced, leading to an increase in NH_3 production and Faraday efficiency (Fig. 4e). This was due to the utilization of thermal energy to surmount the thermodynamic barriers in the reaction pathways. Furthermore, the reaction rate for the formation of *H on Ni single atoms was quantified through in $situ$ SI-SECM measurements to explain the increased selectivity of the Ni_1Cu SAAO catalyst. More specifically, the authors used the catalyst-loaded substrate to determine the *H concentration when the Cu_2O NWs and Ni_1Cu SAAO were biased at different potentials. The catalytic substrate was first biased at a reducing potential $E_{substrate}$ to generate *H. After this, the system was restored to open-circuit conditions so that *H was neither generated nor consumed, and the redox reaction of the redox mediator FcMeOH (Fc) in the solution could not occur on the substrate. Then an oxidizing potential was biased on the UME to oxidize Fc to Fc$^+$. Fc$^+$ can be reduced to Fc by *H on the

substrate, generating a positive feedback current on the UME until all *H were consumed by Fc^+, and the surface concentration of *H could be obtained from the charges transferred during the process. As $E_{substrate}$ became more negative in the first step, more *H were generated on the substrate (Fig. 4f). Remarkably, the concentration of *H on the Ni_1Cu SAAO catalyst was four times greater than that on Cu_2O NWs when $E_{substrate}$ was −0.4 V *vs.* RHE. Moreover, *H production signals were seen in Ni_1Cu SAAO at a more positive potential of around 0.05 V *vs.* RHE, indicating a considerable increase in water dissociation upon the addition of Ni single atoms. These results were also supported by the results of DFT calculations and *in situ* Raman spectroscopy, confirming that the addition of single-atom Ni sites greatly increases the hydrogen adsorption capacitance of Ni_1Cu SAAO.

SECM-based study of the CO_2RR using alternative approach curves

One environmentally friendly way to achieve the goal of carbon neutrality is the electrochemical reduction of CO_2 (CO_2RR) into chemicals with added value using electricity from renewable sources. This process also addresses the intermittent nature of renewable electricity generation.[104–108] An additional benefit is that the electrochemical CO_2 reduction process operates at room temperature and pressure and may be adjusted by varying the applied potential,[109] making the reaction conditions environmentally friendly. These factors enable the use of this technology in scale-up applications. SECM has been widely used in the field of the CO_2RR at present,[68,69,72,110–112] and alternative approach curves played crucial roles in these studies where the conventional approach curves fell short.

Recently, with the development of UME-based pH-sensors, the quantitative analysis of the local pH during the CO_2RR has been achieved using SECM, providing insight into the CO_2RR mechanism.[72,110] For instance, Koper *et al.* designed a UME-based voltammetric pH sensor to measure the pH in the diffusion layer during CO_2 reduction through SECM.[72] The Au UME was functionalized with the 4-hydroxylaminothiophenol (4-HATP)/4-nitrosothiophenol (4-NSTP) redox couple. Since a proton was involved in the redox reaction of 4-HATP/4-NSTP, according to the Nernst equation, the formal potential of the redox reaction obtained from CV (Fig. 5a) had a linear relationship with pH, and the calibration curve was obtained in solutions with different pH values (Fig. 5b). Up to pH 3.45, the calibration curves under the argon and CO_2 atmospheres overlapped, while the calibration curve under a CO_2 atmosphere reached a plateau at higher pH. This was due to the formation of CO_2-saturated solutions under a CO_2 atmosphere, with a stable pH of about 4. To position the Au UME near the electrode surface, the capacitance-based approach curve was applied, and the Au UME was positioned 80 ± 2 μm from the surface of a polycrystalline gold disc. The local pH during the CO_2RR was measured using tip voltammetry at 4 s/data point while the reaction on the gold disc electrode was switched 'on' and 'off' by stepping the potential from −0.5 to −0.9 V *vs.* Ag/AgCl in 50 mV steps, with a potential of 0 V applied during potential steps. The
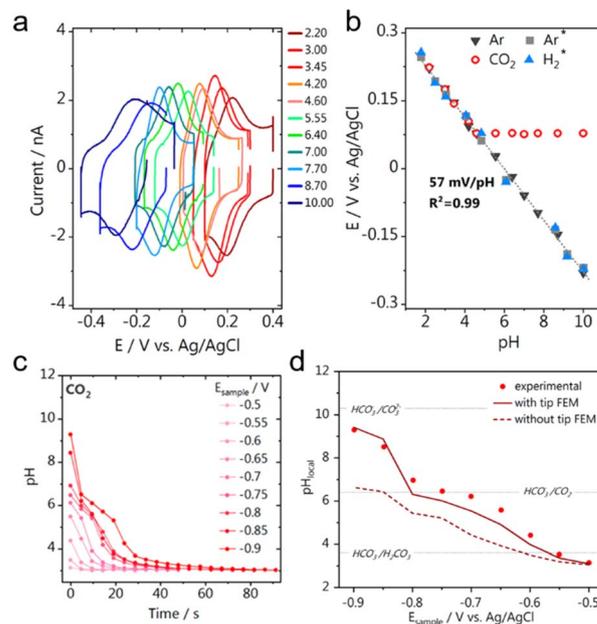

Fig. 5 (a) CVs on the Au-UME in 0.1 M Li_2SO_4 solutions with different pH values. Scan rate: 200 mV s^{-1}. (b) Calibration curves between pH and the formal potential recorded from the Au UME pH sensor under different atmospheres. The calibration curves from previous work (grey square for Ar and blue triangle for H_2) are also shown for comparison. (c) The pH recovery profile recorded on the Au UME after the CO_2RR was turned "off" by setting the potential to 0 V *vs.* Ag/AgCl. Before the CO_2RR on the substrate was turned off, the substrate was biased at different sample potentials E_{sample} (*vs.* Ag/AgCl). (d) Experimental (red dots) and simulated (red lines) local pH values at the Au-UME after the substrate was biased at different E_{sample} to drive the CO_2RR. The local pH values when the Au-UME was positioned close to the substrate ($L = 3.4$, dark red solid line) and when the Au-UME was positioned far from the substrate ($L = 50$, dark red dashed line) were both simulated. Bulk CO_2 concentration was fixed at 10 mM. L is the normalized tip–surface separation. Reproduced with permission from ref. 69, American Chemical Society, 2021.

authors focused on the interfacial pH recovery profile once the reaction was turned 'off' by stepping the potential on the gold disc back to 0 V (Fig. 5c), where no electrochemical reactions occurred. The monitored pH recovery was heavily affected by the hindered diffusion of OH^- with an UME positioned in the diffusion layer, as illustrated in Fig. 5d. According to the finite element method (FEM) simulation, when the Au UME was positioned close to the substrate ($L = 3.4$, L being the tip–substrate distance), the OH^- concentration at the Au UME surface was significantly higher than the case when the Au UME was positioned far from the substrate ($L = 50$). Additionally, a good fit between the experimental result and the simulated pH profile demonstrated that the diffusion hindrance caused by the UME was well-accounted for. Additionally, another UME-based voltammetric pH-sensor was used as the SECM probe to detect the local pH changes during the CO_2RR from the $Cu_xO_yC_z$ nanostructured electrocatalysts.[110] A Pt UME (diameter < 1 μm) was positioned ~100 nm from the $Cu_xO_yC_z$-coated GDE surface by the shear-force-based SECM approach curve, and the local OH^- concentration near the catalyst surface was monitored as

the formal potential of the redox reaction of Pt/PtO on the UME had a linear correlation with OH^- concentration.

Monteiro et al. devised a technique to probe the local activity of GDEs under operando conditions utilizing SECM and Au UME ($r = 1$ μm) (Fig. 6a and b).[69] They examined the effects of CO_2 back-pressure and catalyst loading on the local activity of Au-GDEs (3 cm^2 in size) at various applied potentials. Catalysts were loaded onto GDEs with a loading gradient, so that a GDE surface with low to high catalyst-loading densities was used as the substrate, and the Au UME was positioned close to 100 nm from the GDE using the shear force-based approach curve, which was otherwise impractical using conventional approach curves due to the surface roughness of the GDE. The CO_2RR activity on the GDE was probed using the SG/TC mode of SECM, where CO was produced on the GDE and oxidized at the Au UME, and by moving the Au UME laterally above the GDE, the activity at locations with different loading densities could be mapped. In order to maximize the performance of GDEs, the applied sample potential and the CO_2 back-pressure were adjusted simultaneously, and the interaction between catalyst loading and CO_2 back-pressure was assessed from the current signal on the Au UME. It was found that higher catalyst loadings lead to enhanced CO_2RR activity in the presence of sufficient CO_2, while the situation was more complicated for the CO_2 back-pressure. An optimal CO_2 back-pressure was required to reach maximum CO_2RR activity, which was dependent on the catalyst loading density. Additionally, Fig. 6c–e display the activity maps at various GDE potentials, with more CO generated at more negative potentials. It is worth noting that significant variations in the GDE activity over the scanned region were observed, indicating the inhomogeneity of the lateral response throughout the GDEs. This should not be caused by a variation in the catalyst loading density as the catalyst gradient was produced over a significantly larger length of the GDE (1.7 cm) than the length of the lateral scan in Fig. 6c–e (30 μm). As observed by SEM, a considerable number of larger holes existed on the surface of the GDE, which might contribute to the notable variations in activity. The varying results demonstrated that, in addition to a high catalyst loading, sufficient CO_2 supply and a uniform distribution of GDE pores accessible to CO_2 were necessary to produce a three-phase reaction boundary.

Koper et al. used CV measurements to study the CO_2RR on 5 mm diameter gold disc electrodes using the hanging meniscus configuration, and found that the CO_2RR did not occur in a pure H_2SO_4 electrolyte in the absence of a metal cation.[111] To confirm this and to extend the study to silver and copper electrodes, the CO_2RR near the substrate with and without the presence of metal cations was monitored using the SG/TC mode of SECM with a Pt UME ($r = 6.5 \pm 0.07$ μm) (Fig. 7a). As shown in Fig. 7b, on the gold substrate only hydrogen oxidation (H_{2ox}) occurred under an argon atmosphere. In comparison, under a CO_2 atmosphere, a strong peak owing to the oxidation of CO (CO_{ox}) appeared when Cs^+ was introduced into the electrolyte, while this peak was not observed in the absence of Cs^+. Similar outcomes were observed on silver and copper electrodes, where the CO_2RR occurred only in the presence of Cs^+ under a CO_2 atmosphere (Fig. 7c and d). In
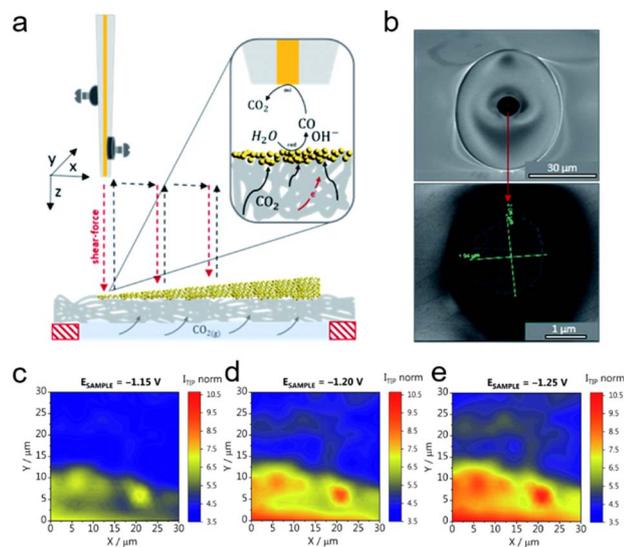

Fig. 6 (a) Schematic representation of the SECM experimental setup, with the Au UME mounted on the piezo, approaching the GDE coated with catalysts using the capacitance-based approach curve. After the Au UME was positioned near the GDE, the CO_2RR activity was characterized in the SG-TC mode, as shown in the inset. (b) SEM micrographs of the Au UME. (c–e) Activity maps recorded for the GDE at a CO_2 back-pressure of 0.7 mbar. The GDE potentials were reported versus Ag/AgCl/3 M KCl in 1 M $KHCO_3$. The tip current (I_{tip} norm) was normalized to the double-layer charging current recorded at −0.6 V. Reproduced with permission from ref. 69, Royal Society of Chemistry, 2021.
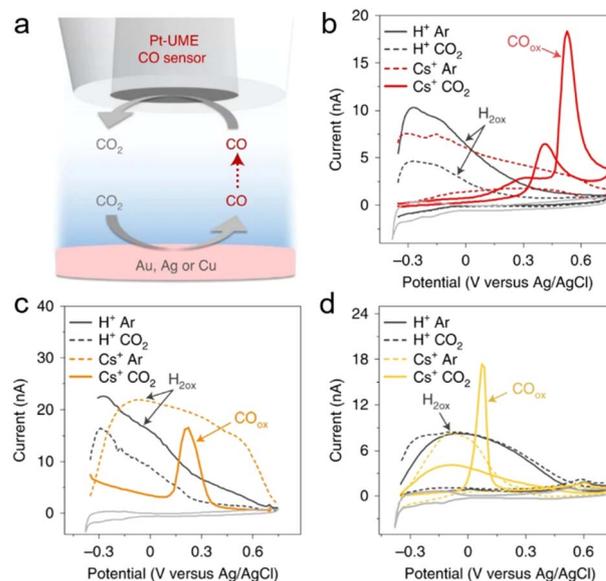
Fig. 7 (a) Schematic representation of the SECM experiment. (b) CV on the Pt UME obtained directly after CO_2 reduction on gold electrodes. (c) CV on the Pt UME obtained directly after CO_2 reduction on silver electrodes. (d) CV on the Pt UME obtained directly after CO_2 reduction on copper electrodes. The CVs on the Pt-UME before applying any potential to the sample are shown in light grey for reference. Reproduced with permission from ref. 111, Nature, 2021.

conclusion, on gold, silver, or copper electrodes, CO was only identified under a CO_2 atmosphere, and only after the electrolyte had been supplemented with Cs^+. Through DFT calculations, the authors found that Cs^+, as well as other alkaline metal ions, were partially desolvated in the $Au–H_2O–M^+$ system (M^+ being the metal ion), and had three promotional effects for the CO_2RR. Namely, the existence of Cs^+ helped stabilize the CO_2 adsorption on the catalyst through the electrostatic interaction between Cs^+ and an oxygen atom in CO_2. The partially desolvated Cs^+ also decreased the O–C–O angle from 180° to 140°, activating the CO_2 molecule. Lastly, the partially desolvated Cs^+ enhanced the electron transfer from the catalytic surface to CO_2. Overall, using CV and SECM, the authors demonstrated that positively charged species from the electrolyte were essential for the CO_2RR, and the underlying mechanism was explained by DFT calculations.

SECM-based detection of short-lived reactive oxygen species

Reactive oxygen species (ROS) refer to a group of chemically active substances containing oxygen atoms,[113–116] including singlet oxygen ($^1O_2$), hydrogen peroxide (H_2O_2), hydroxyl radicals ($^\bullet OH$), and superoxide anion radicals ($O_2^{\bullet-}$). ROS participate in a variety of chemical and biological processes, such as energy metabolism, cell signalling, and antioxidant defence.[117,118] Nonetheless, detection of certain ROS, such as $^1O_2$, $^\bullet OH$, and $O_2^{\bullet-}$ remains challenging due to their short lifetime and high reactivity.[119–129]

Known for its high reactivity, strong oxidative properties, and short lifetime, it is challenging to detect $^\bullet OH$. Traditionally, $^\bullet OH$ can be detected using electron spin resonance (ESR) with the help of spin traps such as 5,5-dimethyl-1-pyrroline N-oxide (DMPO), yet this method suffers from an unsatisfactory sensitivity and is inconvenient to measure the generation process of $^\bullet OH$ in real time. To solve these issues, Rodríguez-López's group proposed a novel method for detecting $^\bullet OH$ at operating electrodes.[123] The authors discovered that the $[DMPO–OH]^\bullet$ adduct, formed by the reaction of $^\bullet OH$ with DMPO, was stable in the aqueous solution and was redox-active with a formal potential of 0.85 V *vs.* Ag/AgCl. Electrodes of various materials were tested to electrochemically generate $^\bullet OH$ and the boron-doped diamond (BDD) was found to be the most effective one. Thus, using SECM, the freshly generated $[DMPO–OH]^\bullet$ adduct from a BDD electrode surface was detected with a UME (12.5 μm in radius) positioned 10 μm from the BDD electrode using SECM (Fig. 8a).

Furthermore, the Rodríguez-López group studied ROS formation from a Fe–N–C catalyst during the ORR in real-time using the SG/TC mode of SECM.[130] Specifically, the $[DMPO–OH]^\bullet$ adduct generated near the Fe–N–C catalyst was detected using Au UMEs with a diameter of 25 μm at a tip–substrate distance of approximately 10 μm, while H_2O_2 generated near the catalysts was collected using Pt UMEs ($d = 25$ μm). As the substrate was biased at more and more negative potentials, more $^\bullet OH$ was generated, yet H_2O_2 production reached a peak when the substrate was biased at ~0.55 V *vs.* Ag/AgCl (Fig. 8b and c). The different behaviors of $^\bullet OH$ and H_2O_2 with varying substrate potential were due to $^\bullet OH$ being the predominant
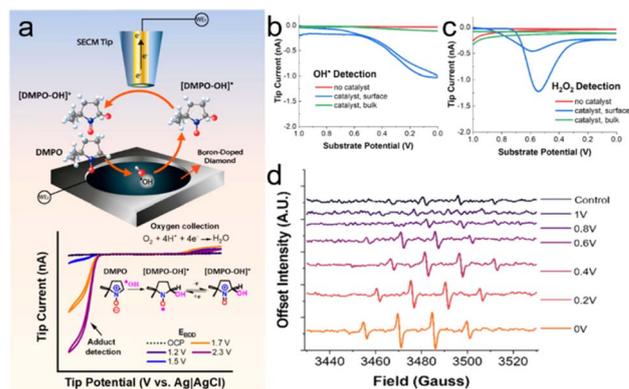

Fig. 8 (a) Detection of the $[DMPO–OH]^\bullet$ adduct formed from spin trapping of $^\bullet OH$ radicals generated on BDD electrodes at different applied potentials (E_{BDD}) using SECM. Reproduced with permission from ref. 123, American Chemical Society, 2022. (b) The radical detection response collected at the gold tip as the substrate potential was swept at 10 mV s^{-1} with 25 mM DMPO in solution. (c) The H_2O_2 detection response collected at a Pt tip as the substrate potential was swept at 10 mV s^{-1}. (d) ESR spectra of 50 mM DMPO after two minutes of electrolysis at the pyrolyzed Fe–N–C catalyst substrate at increasingly reducing potentials. Reproduced with permission from ref. 130, Royal Society of Chemistry, 2024.

radical species, as confirmed by *ex situ* ESR measurements (Fig. 8d). Overall, real-time measurements of difficult-to-observe free radical intermediates and by-products using SECM were helpful in identifying the mechanistic variations among various electrocatalytic materials for the ORR and other processes.

Conclusions and outlook

In this perspective, the recent advances in the development of SECM operation modes were summarized. Using shear-force-based and capacitance-based approach curves, SECM tips could be positioned near the surface of non-flat electrodes, benefiting the characterization of catalysts under operating conditions. The SI-SECM technique proves to be a powerful tool for detecting the surface active site densities, as well as determining the reaction rates of the surface adsorption process. Also, the development of potentiometric SECM probes opens up the opportunity to study local pH near the substrate at the microscopic level. All of these expanded the functionality of SECM, and SECM-based progress has been made in new scenarios, such as electrocatalytic reactions including the NO_3RR, NRR, CO_2RR and so on, quantifying the catalytic properties of the catalysts and providing insights into the reaction mechanisms.

Despite recent advancements in SECM-based studies of electrocatalytic reactions, critical challenges persist in achieving quantitative kinetic information and unveiling the reaction mechanisms. The first issue is obtaining a precise tip–substrate distance when the substrate is not ideally flat, which is often the case when the substrate is loaded with nanoparticles of electrocatalysts. In SECM studies, the mass transfer towards the tip is greatly controlled by the tip–substrate

distance. Thus, the current signal on the tip in SG/TC modes is not only a function of the reaction kinetics, but also largely affected by the tip–substrate distance. A precise and quantitative control of the tip–substrate distance is crucial for the quantitative study of catalytic reaction kinetics. When the substrate is flat, the tip–substrate distance can be well-controlled by comparing the approach curves with the theory, yet the approach curve over a non-flat surface such as a GDE is much more complicated and usually cannot be analyzed quantitatively. Even though UMEs could be brought to a few hundred nanometers above a rough substrate using the shear-force-based approach curves, a quantitative tip–substrate distance is missing, making the analysis of reaction kinetics difficult.

The second issue is spatial resolution, which is limited by the UMEs. Although smaller UMEs have been developed, a large amount of work still prefers UMEs with 10–25 μm diameter so far. Typically, electrocatalysts tens to hundreds of nanometers in size were used, which were far beyond the spatial resolution provided by these UMEs. Usually, a smaller probe size leads to a better spatial resolution. However, experiments with smaller UMEs get much more challenging, and special care must be taken to properly handle the tip and the potentiostat,[131,132] as well as to minimize thermal drift caused by temperature fluctuations near the tip.[133]

The third challenge arises from the complicated mechanisms of multi-electron transfer reactions, including the NRR, NO_3RR, and CO_2RR. These processes involve intertwined proton-coupled electron transfer (PCET) steps, competitive adsorption of intermediates, and potential-dependent selectivity bifurcations, and have multiple potential products. A lot of effort is required to acquire the selectivity towards different reaction pathways and the kinetics of each step. Moreover, the adsorption processes may play critical roles in these reactions. Using SECM, complicated reaction mechanisms involving adsorption and multiple electron transfer steps have been unveiled,[134] yet the adsorption process is barely considered in current SECM-based electrocatalysis studies.

The further development of SECM-related theories, instrumental innovation and coupling SECM with other analytical methods would be helpful to tackle these challenges. Finite element simulation combined with machine learning might help to provide a numerical solution to the theoretical approach curve over a non-flat substrate, enabling a quantitative positioning of UME on *operando* electrodes like the GDE. Multiscale modeling combining DFT-calculation, finite element simulations of intermediate surface concentration, and microkinetic analysis of PCET steps would shed light on the complicated reaction mechanisms during multi-electron transfer reactions like the NRR, NO_3RR, and CO_2RR. The development of smaller UMEs as well as protocols of using these UMEs will help to greatly improve the spatial resolution of SECM-based studies.[135] And coupling *in situ* electrochemical measurements with other analytical techniques would lead to more information about reaction mechanisms. For example, by coupling a rotating disk electrode with Raman spectroscopy and infrared spectroscopy, information on the adsorption of protons on noble metals has

been revealed.[136,137] Coupling CV with mass spectrometry provided structural information of the intermediates during electron transfer reactions, and can help to identify the reaction pathways.[138] Overall, progress in the above-mentioned fields will boost our understanding of the electrocatalytic reactions and facilitate the pursuit for sustainable and renewable energy.

Data availability

No primary research results, software or code have been included and no new data were generated or analysed as part of this review.

Author contributions

Conflicts of interest

There are no conflicts to declare.

Acknowledgements

References

1 J. Lelieveld, K. Klingmüller, A. Pozzer, R. T. Burnett, A. Haines and V. Ramanathan, *Proc. Natl. Acad. Sci. U. S. A.*, 2019, **116**, 7192–7197.

2 K. Kohse-Höinghaus, *Chem. Rev.*, 2023, **123**, 5139–5219.

3 S. R. Nicholson, N. A. Rorrer, A. C. Carpenter and G. T. Beckham, *Joule*, 2021, **5**, 673–686.

4 A. A. Lacis, G. A. Schmidt, D. Rind and R. A. Ruedy, *Science*, 2010, **330**, 356–359.

5 J. Masa, C. Andronescu and W. Schuhmann, *Angew. Chem., Int. Ed.*, 2020, **59**, 15298–15312.

6 C. Long, J. Han, J. Guo, C. Yang, S. Liu and Z. Tang, *Chem Catal.*, 2021, **1**, 509–522.

7 H. Zhang, M. Zhu, O. G. Schmidt, S. Chen and K. Zhang, *Adv. Energy Sustainability Res.*, 2021, **2**, 2000090.

8 A. Kumar, V. K. Vashistha, D. K. Das, S. Ibraheem, G. Yasin, R. Iqbal, T. A. Nguyen, R. K. Gupta and M. Rasidul Islam, *Fuel*, 2021, **304**, 121420.

9 Y. Yang, C. R. Peltier, R. Zeng, R. Schimmenti, Q. Li, X. Huang, Z. Yan, G. Potsi, R. Selhorst, X. Lu, W. Xu, M. Tader, A. V. Soudackov, H. Zhang, M. Krumov, E. Murray, P. Xu, J. Hitt, L. Xu, H. Y. Ko, B. G. Ernst, C. Bundschu, A. Luo, D. Markovich, M. Hu, C. He, H. Wang, J. Fang, R. A. DiStasio, L. F. Kourkoutis, A. Singer, K. J. T. Noonan, L. Xiao, L. Zhuang, B. S. Pivovar, P. Zelenay, E. Herrero, J. M. Feliu, J. Suntivich, E. P. Giannelis, S. Hammes-Schiffer, T. Arias,

M. Mavrikakis, T. E. Mallouk, J. D. Brock, D. A. Muller, F. J. DiSalvo, G. W. Coates and H. D. Abruña, *Chem. Rev.*, 2022, **122**, 6117–6321.

10 C. A. Campos-Roldán, D. J. Jones, J. Rozière and S. Cavaliere, *ChemCatChem*, 2022, **14**, e202200334.

11 G. Russo, *Nature*, 2014, **513**, 478–480.

12 A. K. Sleiti, *Renewable Sustainable Energy Rev.*, 2017, **69**, 435–441.

13 M. Roeb and H. Müller-Steinhagen, *Science*, 2010, **329**, 773–774.

14 H. Zhang and J. Yan, *Joule*, 2022, **6**, 1142–1144.

15 H. Zhao and Z. Yuan, *Adv. Energy Mater.*, 2023, **13**, 2300254.

16 J. T. Ren, L. Chen, H. Y. Wang, W. W. Tian and Z. Y. Yuan, *Energy Environ. Sci.*, 2024, **17**, 49–113.

17 Z. Chen, S. Yun, L. Wu, J. Zhang, X. Shi, W. Wei, Y. Liu, R. Zheng, N. Han and B. J. Ni, *Nano-Micro Lett.*, 2023, **15**, 4.

18 T. Li, P. Wang, M. He, T. Zhang, C. Yang and Z. Li, *Coord. Chem. Rev.*, 2024, **521**, 216179.

19 B. A. Yusuf, W. Yaseen, S. Meng, J. Xie, F. O. Fapohunda, R. Nankya, A. I. Muhammad, M. Xie and Y. Xu, *Coord. Chem. Rev.*, 2023, **492**, 215273.

20 J. Zhang, J. Ding, Y. Liu, C. Su, H. Yang, Y. Huang and B. Liu, *Joule*, 2023, **7**, 1700–1744.

21 H. Zhang, K. Fang, J. Yang, H. Chen, J. Ning, H. Wang and Y. Hu, *Coord. Chem. Rev.*, 2024, **506**, 215723.

22 F. Y. Chen, A. Elgazzar, S. Pecaut, C. Qiu, Y. Feng, S. Ashokkumar, Z. Yu, C. Sellers, S. Hao, P. Zhu and H. Wang, *Nat. Catal.*, 2024, **7**, 1032–1043.

23 Y. Xiong, Y. Wang, J. Zhou, F. Liu, F. Hao and Z. Fan, *Adv. Mater.*, 2024, **36**, 2304021.

24 H. F. Wang, L. Chen, H. Pang, S. Kaskel and Q. Xu, *Chem. Soc. Rev.*, 2020, **49**, 1414–1448.

25 Y. Lin, Y. Dong, X. Wang and L. Chen, *Adv. Mater.*, 2023, **35**, 2210565.

26 S. Dey, B. Mondal, S. Chatterjee, A. Rana, S. Amanullah and A. Dey, *Nat. Rev. Chem.*, 2017, **1**, 0098.

27 J. Li, S. U. Abbas, H. Wang, Z. Zhang and W. Hu, *Nano-Micro Lett.*, 2021, **13**, 216.

28 X. Zhao, G. Hu, G. Chen, H. Zhang, S. Zhang and H. Wang, *Adv. Mater.*, 2021, **33**, 2207650.

29 Z. Zhang, J. Liu, Y. Xu, C. Xie, S. Wang and X. Yao, *Chem. Soc. Rev.*, 2024, **53**, 10620–10659.

30 P. Sebastián-Pascual and M. Escudero-Escribano, *ACS Energy Lett.*, 2020, **5**, 130–135.

31 W. Ge, Y. Chen, Y. Fan, Y. Zhu, H. Liu, L. Song, Z. Liu, C. Lian, H. Jiang and C. Li, *J. Am. Chem. Soc.*, 2022, **144**, 6613–6622.

32 Z. Kou, X. Li, L. Zhang, W. Zang, X. Gao and J. Wang, *Small Sci.*, 2021, **1**, 2100011.

33 E. P. Alsaç, N. Bodappa, A. W. H. Whittingham, Y. Liu, A. D. Lazzari and R. D. L. Smith, *Chem. Phys. Rev.*, 2021, **2**, 031306.

34 E. Fabbri, M. Nachtegaal, T. Binninger, X. Cheng, B. J. Kim, J. Durst, F. Bozza, T. Graule, R. Schäublin, L. Wiles, M. Pertoso, N. Danilovic, K. E. Ayers and T. J. Schmidt, *Nat. Mater.*, 2017, **16**, 925–931.

35 X. Qin, S. Zhu, F. Xiao, L. Zhang and M. Shao, *ACS Energy Lett.*, 2019, **4**, 1778–1783.

36 D. Polcari, P. Dauphin-Ducharme and J. Mauzeroll, *Chem. Rev.*, 2016, **116**, 13234–13278.

37 M. Shen, R. Ishimatsu, J. Kim and S. Amemiya, *J. Am. Chem. Soc.*, 2012, **134**, 9856–9859.

38 R. Chen, P. Pathirathna, R. J. Balla, J. Kim and S. Ameyiya, *Anal. Chem.*, 2024, **96**, 10765–10771.

39 Y. Li, X. Ning, Q. Ma, D. Qin and X. Lu, *TrAC, Trends Anal. Chem.*, 2016, **80**, 242–254.

40 T. Kai, M. Zhou, S. Johnson, H. S. Ahn and A. J. Bard, *J. Am. Chem. Soc.*, 2018, **140**, 16178–16183.

41 M. Zhou, Y. Yu, K. Hu and M. V. Mirkin, *J. Am. Chem. Soc.*, 2015, **137**, 6517–6523.

42 T. Kai, M. Zhou, Z. Duan, G. A. Henkelman and A. J. Bard, *J. Am. Chem. Soc.*, 2017, **139**, 18552–18557.

43 Y. Yang, Y. Xiong, R. Zeng, X. Lu, M. Krumov, X. Huang, W. Xu, H. Wang, F. J. DiSalvo, J. D. Brock, D. A. Muller and H. D. Abruña, *ACS Catal.*, 2021, **11**, 1136–1178.

44 M. A. Bhat, N. Nioradze, J. Kim, S. Amemiya and A. J. Bard, *J. Am. Chem. Soc.*, 2017, **139**, 15891–15899.

45 R. Chen, S. Liu and Y. Zhang, *Mater. Horiz.*, 2023, **10**, 52–64.

46 K. Barman, X. Wang, R. Jia and M. V. Mirkin, *J. Am. Chem. Soc.*, 2021, **143**, 8547–8551.

47 J. Clausmeyer and W. Schuhmann, *TrAC, Trends Anal. Chem.*, 2016, **79**, 46–59.

48 J. Zhang, Y. Liu, Y. Li, T. Zhu, J. Qiu, F. Xu, H. Zhang and F. Li, *Small Methods*, 2016, **6**, 2200689.

49 J. Timoshenko and B. R. Cuenya, *Chem. Rev.*, 2021, **121**, 882–961.

50 M. Rüscher, A. Herzog, J. Timoshenko, H. S. Jeon, W. Frandsen, S. Kühl and B. R. Cuenya, *Catal. Sci. Technol.*, 2022, **12**, 3028–3043.

51 H. J. Niu, Y. Yan, S. Jiang, T. Liu, T. Sun, W. Zhou, L. Guo and J. Li, *ACS Nano*, 2022, **16**, 11049–11058.

52 A. Djire, X. Wang, C. Xiao, O. C. Nwamba, M. V. Mirkin and N. R. Neale, *Adv. Funct. Mater.*, 2020, **30**, 2001136.

53 G. Li, T. Sun, H. Niu, Y. Yan, T. Liu, S. Jiang, Q. Yang, W. Zhou and L. Guo, *Adv. Funct. Mater.*, 2023, **33**, 2212514.

54 Z. Wang, R. Liu, T. Sun, M. Li, N. Ran, D. Wang and Z. Wang, *Anal. Chem.*, 2024, **96**, 7618–7625.

55 H. Niu, C. Huang, T. Sun, Z. Fang, X. Ke, R. Zhang, N. Ran, J. Wu, J. Liu and W. Zhou, *Angew. Chem., Int. Ed.*, 2024, **63**, e202401819.

56 C. Iffelsberger and M. Pumera, *J. Mater. Chem. A*, 2021, **9**, 22072–22081.

57 Z. Wang, T. Sun, C. HuangFu, S. Jiang, C. Gu, L. Jiao and Z. Wang, *Nano Res.*, 2023, **16**, 10011–10017.

58 S. Jiang, T. Sun, C. Gu, Y. Ma, Z. Wang, D. Wang and Z. Wang, *Nano Res.*, 2023, **16**, 8902–8909.

59 L. Lan, Y. Wu, Y. Pei, Y. Wei, T. Hu, D. Lützenkirchen-Hecht, K. Yuan and Y. Chen, *Adv. Mater.*, 2025, **37**, 2417711.

60 S. Kaur, K. Garg and T. C. Nagaigh, *ACS Energy Lett.*, 2025, **10**, 1430–1438.

61 J. L. Fernández and A. J. Bard, *Anal. Chem.*, 2004, **76**, 2281–2289.

62 C. M. Sánchez-Sánchez, J. Rodríguez-López and A. J. Bard, *Anal. Chem.*, 2008, **80**, 3254–3260.

63 B. B. Katemann, A. Schulte and W. Schuhmann, *Chem.–Eur. J.*, 2003, **9**, 2025–2033.

64 J. Park, J. H. Lim, J. H. Kang, J. Lim, H. W. Jang, H. Shin and S. H. Park, *J. Energy Chem.*, 2024, **91**, 155–177.

65 T. B. Clarke, L. E. Krushinski, K. J. Vannoy, G. Colón-Quintana, K. Roy, A. Rana, C. Renault, M. L. Hill and J. E. Dick, *Chem. Rev.*, 2024, **124**, 9015–9080.

66 Z. Jin, P. Li, Y. Meng, Z. Fang, D. Xiao and G. Yu, *Nat. Catal.*, 2021, **4**, 615–622.

67 P. Li, Z. Jin, Z. Fang and G. Yu, *Energy Environ. Sci.*, 2021, **14**, 3522–3531.

68 Y. Nam, S.-E. Cho and H. S. Ahn, *ACS Catal.*, 2024, **14**, 17084–17089.

69 M. C. O. Monteiro, S. Dieckhöfer, T. Bobrowski, T. Quast, D. Pavesi, M. T. M. Koper and W. Schuhmann, *Chem. Sci.*, 2021, **12**, 15682–15690.

70 M. C. O. Monteiro, L. Jacobse and M. T. M. Koper, *J. Phys. Chem. Lett.*, 2020, **11**, 9708–9713.

71 M. C. O. Monteiro, L. Jacobse, T. Touzalin and M. T. M. Koper, *Anal. Chem.*, 2020, **92**, 2237–2243.

72 M. C. O. Monteiro, A. Mirabal, L. Jacobse, K. Doblhoff-Dier, S. C. Barton and M. T. M. Koper, *JACS Au*, 2021, **1**, 1915–1924.

73 J. Rodríguez-López, M. A. Alpuche-Avilés and A. J. Bard, *J. Am. Chem. Soc.*, 2008, **130**, 16985–16995.

74 H. S. Ahn and A. J. Bard, *J. Am. Chem. Soc.*, 2016, **138**, 313–318.

75 X. Tang, Y. Zhang, S. Tang, D. Lützenkirchen-Hecht, K. Yuan and Y. Chen, *ACS Catal.*, 2024, **14**, 13065–13080.

76 W. Wu and Y. Wang, *J. Am. Chem. Soc.*, 2025, **147**, 11662–11666.

77 J. Xu, H. Gao, F. Wang and M. Zhou, *Curr. Opin. Electrochem.*, 2023, **39**, 101299.

78 M. Nebel, K. Eckhard, T. Erichsen, A. Schulte and W. Schuhmann, *Anal. Chem.*, 2010, **82**, 7842–7848.

79 B. H. R. Suryanto, H. L. Du, D. Wang, J. Chen, A. N. Simonov and D. R. MacFarlane, *Nat. Catal.*, 2019, **2**, 290–296.

80 D. R. MacFarlane, P. V. Cherepanov, J. Choi, B. H. R. Suryanto, R. Y. Hodgetts, J. M. Bakker, F. M. F. Vallana and A. N. Simonov, *Joule*, 2020, **4**, 1186–1205.

81 J. W. Erisman, M. A. Sutton, J. Galloway, Z. Klimont and W. Winiwarter, *Nat. Geosci.*, 2008, **1**, 636–639.

82 G. Soloveichik, *Nat. Catal.*, 2019, **2**, 377–380.

83 S. L. Foster, S. I. P. Bakovic, R. D. Duda, S. Maheshwari, R. D. Milton, S. D. Minteer, M. J. Janik, J. N. Renner and L. F. Greenlee, *Nat. Catal.*, 2018, **1**, 490–500.

84 X. Xin, Q. Qu, I. E. Khalil, Y. Huang, M. Wei, J. Chen, W. Zhang, F. Huo and W. Liu, *Chin. Chem. Lett.*, 2024, **35**, 108654.

85 J. Zhang, M. Sun, J. Ren, R. Zhang, M. Ma, Q. Xue and J. Tian, *Chin. Chem. Lett.*, 2025, **36**, 110491.

86 C. J. M. van der Ham, M. T. M. Koper and D. G. H. Hetterscheid, *Chem. Soc. Rev.*, 2014, **43**, 5183–5191.

87 A. J. Martín, T. Shinagawa and J. Pérez-Ramírez, *Chem*, 2019, **5**, 263–283.

88 X. Guo, H. Du, F. Qu and J. Li, *J. Mater. Chem. A*, 2019, **7**, 3531–3543.

89 X. Yang, B. Xu, J. G. Chen and X. Yang, *ChemSusChem*, 2023, **16**, e202201715.

90 K. N. Dinh, Q. Liang, C. F. Du, J. Zhao, A. I. Y. Tok, H. Mao and Q. Yan, *Nano Today*, 2019, **25**, 99–121.

91 Z. J. Huba, M. D. Donakowski and A. Epshteyn, *Chem. Mater.*, 2017, **29**, 1467–1471.

92 P. Li, Z. Jin, Z. Fang and G. Yu, *Angew. Chem., Int. Ed.*, 2020, **59**, 22610–22616.

93 J. Kong, H. Kim and H. S. Park, *Appl. Catal., B*, 2023, **338**, 123019.

94 M. Ferrara, M. Bevilacqua, C. Tavagnacco, F. Vizza and P. Fornasiero, *ChemCatChem*, 2020, **12**, 6205–6213.

95 D. Gupta, A. Kafle, M. Singh, D. Dahare and T. C. Nagaiah, *J. Mater. Chem. A*, 2023, **11**, 24812–24822.

96 G. F. Chen, Y. Yuan, H. Jiang, S. Y. Ren, L. X. Ding, L. Ma, T. Wu, J. Lu and H. Wang, *Nat. Energy*, 2020, **5**, 605–613.

97 P. H. van Langevelde, I. Katsounaros and M. T. M. Koper, *Joule*, 2021, **5**, 290–294.

98 P. Li, R. Li, Y. Liu, M. Xie, Z. Jin and G. Yu, *J. Am. Chem. Soc.*, 2023, **145**, 6471–6479.

99 K. Liu, H. Li, M. Xie, P. Wang, Z. Jin, Y. Liu, M. Zhou, P. Li and G. Yu, *J. Am. Chem. Soc.*, 2024, **146**, 7779–7790.

100 H. Li, S. Li, R. Guan, Z. Jin, D. Xiao, Y. Guo and P. Li, *ACS Catal.*, 2024, **14**, 12042–12050.

101 P. Li, L. Liao, Z. Fang, G. Su, Z. Jin and G. Yu, *Proc. Natl. Acad. Sci. U. S. A.*, 2023, **120**, e2305489120.

102 P. Li, Z. Jin, Z. Fang and G. Yu, *Energy Environ. Sci.*, 2021, **14**, 3522–3531.

103 C. Park, M. Y. Seo, T. Kwon, J. Kim, K. M. Nam, Y. K and J. Chang, *J. Am. Chem. Soc.*, 2025, **147**, 687–700.

104 S. Nitopi, E. Bertheussen, S. B. Scott, X. Liu, A. K. Engstfeld, S. Horch, B. Seger, I. E. L. Stephens, K. Chan, C. Hahn, J. K. Nørskov, T. F. Jaramillo and I. Chorkendorff, *Chem. Rev.*, 2019, **119**, 7610–7672.

105 S. Pacala and R. Socolow, *Science*, 2004, **305**, 968–972.

106 P. D. Luna, C. Hahn, D. Higgins, S. A. Jaffer, T. F. Jaramillo and E. H. Sargent, *Science*, 2019, **364**, 6438.

107 X. Wang, Y. Wang, L. Cui, W. Gao, X. Li, H. Liu, W. Zhou and J. Wang, *Chin. Chem. Lett.*, 2024, **35**, 110031.

108 X. Jiang, Y. Zhao, Y. Kong, J. Sun, S. Feng, X. Lu, Q. Hu, H. Yang and C. He, *Chin. Chem. Lett.*, 2025, **36**, 109555.

109 D. D. Zhu, J. L. Liu and S. Z. Qiao, *Adv. Mater.*, 2016, **28**, 3423–3452.

110 N. Sikdar, J. R. C. Junqueira, S. Dieckhöfer, T. Quast, M. Braun, Y. Song, H. B. Aiyappa, S. Seisel, J. Weidner, D. Öhl, C. Andronescu and W. Schuhmann, *Angew. Chem., Int. Ed.*, 2021, **60**, 23427–23434.

111 M. C. O. Monteiro, F. Dattila, B. Hagedoorn, R. García-Muelas, N. López and M. T. M. Koper, *Nat. Catal.*, 2021, **4**, 654–662.

112 Y. K. Yesudas, M. Balamurugan, K. T. Nam, B. Gopal and A. S. Kumar, *J. Mater. Chem. A*, 2024, **12**, 31135–31144.

113 Y. Zhang, M. Dai and Z. Yuan, *Anal. Methods*, 2018, **10**, 4625–4638.

114 J. Wu, Y. Zhao, K. Li, S. Muhammad, M. Ju, L. Liu, Y. Huang, B. Wang, W. Ding, B. Shen and H. Huang, *TrAC, Trends Anal. Chem.*, 2022, **157**, 116734.

115 F. Yan, Y. Zang, J. Sun, Z. Sun and H. Zhang, *TrAC, Trends Anal. Chem.*, 2020, **131**, 116009.

116 N. Kwon, D. Kim, K. M. K. Swamy and J. Yoon, *Coord. Chem. Rev.*, 2021, **427**, 213581.

117 Y. Su, H. Song and Y. Lv, *Microchem. J.*, 2019, **146**, 83–97.

118 D. Wang, L. Zhao, L. H. Guo and H. Zhang, *Anal. Chem.*, 2014, **86**, 10535–10539.

119 W. Yu and L. Zhao, *TrAC, Trends Anal. Chem.*, 2021, **136**, 116197.

120 C. Iffelsberger, T. Raith, P. Vatsyayan, V. Vyskočil and F. M. Matysik, *Electrochim. Acta*, 2018, **281**, 494–501.

121 X. Zhao, S. Lam, J. Jass and Z. Ding, *Electrochem. Commun.*, 2010, **12**, 773–776.

122 F. P. Filice and Z. Ding, *Analyst*, 2019, **144**, 738–752.

123 J. S. Barroso-Martínez, A. I. B. Romo, S. Pudar, S. T. Putnam, E. Bustos and J. Rodríguez-López, *J. Am. Chem. Soc.*, 2022, **144**, 18896–18907.

124 A. Preet and T. E. Lin, *Catalysts*, 2021, **11**, 594.

125 C. G. Zoski, *J. Electrochem. Soc.*, 2016, **163**, H3088–H3100.

126 P. Bertoncello, *Energy Environ. Sci.*, 2010, **3**, 1620.

127 J. Zhang, Y. Liu, Y. Li, T. Zhu, J. Qiu, F. Xu, H. Zhang and F. Li, *Small Methods*, 2022, **6**, 2200689.

128 A. Latus, J. M. Noël, E. Volanschi, C. Lagrost and P. Hapiot, *Langmuir*, 2011, **27**, 11206–11211.

129 T. Wu, X. Ning, Q. Xiong, F. Zhang and P. He, *Electrochim. Acta*, 2022, **403**, 139638.

130 S. T. Putnam and J. Rodríguez-López, *Chem. Sci.*, 2024, **15**, 10036–10045.

131 N. Nioradze, R. Chen, J. Kim, M. Shen, P. Santhosh and S. Amemiya, *Anal. Chem.*, 2013, **85**, 6198–6202.

132 J. Kim, B. Kim, S. K. Cho and A. J. Bard, *J. Am. Chem. Soc.*, 2014, **136**, 8173–8176.

133 J. Kim, M. Shen, N. Nioradze and S. Amemiya, *Anal. Chem.*, 2012, **84**, 3489–3492.

134 M. A. Bhat, N. Nioradze, J. Kim, S. Amemiya and A. J. Bard, *J. Am. Chem. Soc.*, 2017, **139**, 15891–15899.

135 J. Kim, C. Renault, N. Nioradze, N. Arroyo-Currás, K. C. Leonard and A. J. Bard, *Anal. Chem.*, 2016, **88**, 10284–10289.

136 S. Zhu, X. Qin, F. Xiao, S. Yang, Y. Xu, Z. Tan, J. Li, J. Yan, Q. Chen, M. Chen and S. Shao, *Nat. Catal.*, 2021, **4**, 711–718.

137 S. Zhu, X. Qin, Y. Yao and S. Shao, *J. Am. Chem. Soc.*, 2020, **142**, 8748–8754.

138 X. Zhang, W. Lu, C. Ma, T. Wang, J. Zhu, R. N. Zare and Q. Min, *Chem. Sci.*, 2022, **13**, 6244–6253.